Journal of Applied Physics ARTICLE pubs.aip.org/aip/jap

Parametric pumping of coherent spin waves by surface acoustic waves

Cite as: J. Appl. Phys. **137**, 073902 (2025); doi: 10.1063/5.0251252
Submitted: 1 December 2024 · Accepted: 21 January 2025 ·
Published Online: 18 February 2025

View Online Export Citation CrossMark

Albrecht Jander,[a] Pallavi Dhagat, and Carson Rivard

AFFILIATIONS

School of Electrical Engineering and Computer Science, Oregon State University, Corvallis, Oregon 97331, USA

Note: This paper is part of the Special Topic, Phonon-Magnon Interactions: From Fundamentals to Device Physics.
[a]**Author to whom correspondence should be addressed:** jander@oregonstate.edu

ABSTRACT

This study investigates the parametric pumping of coherent forward volume spin waves using traveling surface acoustic waves in thin-film yttrium iron garnet. Theoretical analysis, micromagnetic modeling, and experimental validation of the nonlinear three-wave mixing interaction are presented. The energy and momentum imparted by the acoustic pump enable frequency translation and angular deflection of the idler spin waves generated, providing a mechanism for the spectral and spatial separation of signals in magnonic devices. Experimental results demonstrate bilinear parametric interactions, frequency conversion, and angular separation of spin waves under degenerate and nondegenerate conditions and provide evidence of the possibility of parametric amplification of signal spin waves below the instability threshold for generation from the thermal background. The results align qualitatively with theoretical predictions and micromagnetic simulations and lay a path toward developing magnonic signal processing and computing devices utilizing acoustic parametric pumping of spin waves.

I. INTRODUCTION

Spin waves can be amplified by parametric pumping in a region of time-varying magnetic field or anisotropy. This has been demonstrated by pumping spin waves with radio frequency (RF) magnetic fields[1–3] and oscillating anisotropy produced by voltage controlled magnetic anisotropy (VCMA)[4] or standing[5–7] and traveling[8–10] acoustic waves.

Since magnons carry linear momentum, $\hbar\boldsymbol{k}$ (where $\hbar$ is the reduced Planck's constant and $\boldsymbol{k}$ is the wave vector), conservation of momentum dictates that addition of magnons to the signal spin wave must be balanced by the creation of magnons traveling in a different direction, producing the so-called idler wave. In the case of pumping by magnetic field, *standing* acoustic wave or VCMA, the pump does not contribute significant momentum and, thus, conservation of momentum constrains the wave vector of the idler wave to be equal and opposite to that of the signal spin wave. Furthermore, if the spin wave propagation is reciprocal, the frequency of the idler must also be the same as the signal.

If, on the other hand, the pump is a traveling wave carrying momentum of the same order as that of the spin wave, such as an acoustic wave, the idler generated by the interaction may differ in both frequency and wave vector from the original signal. This capability for frequency translation and angular deflection can be advantageous for the spectral and spatial separation of signals in magnonic signal processing devices and computation.

Originally demonstrated in bulk yttrium-iron-garnet (YIG) crystals,[8,9] acoustic parametric pumping of spin waves has seen a resurgence of interest as a method of generating and manipulating spin waves in thin-film magnonic devices. The potential for the amplification and frequency conversion of spin waves by pumping with a surface acoustic wave (SAW) has been established by micromagnetic simulation for backward volume[11] and forward volume[12] spin wave modes. In recent experiments, Geilen *et al.* used Brillouin light scattering to observe spin waves parametrically pumped from the thermal background by SAWs in CoFeB films.[10]

In this work, we explore the parametric pumping of *coherent* forward volume spin waves by a traveling SAW in a thin-film device. Theory, micromagnetic modeling and experimental data of the parametric interaction are presented for ZnO/YIG devices on GGG substrates, as illustrated in Fig. 1. The spin waves are generated and detected by inductive transducers and propagate in the YIG film, a magnetoelastic medium with low spin wave damping.

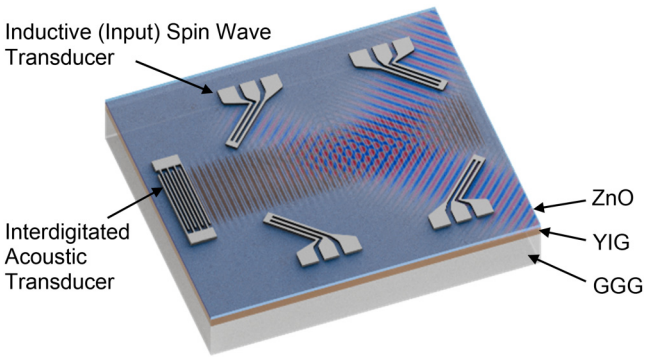

FIG. 1. Schematic of the device for investigating parametric pumping of spin waves by surface acoustic waves. The angle of incidence of the signal spin waves on the acoustic waves is determined by the angle of the input spin wave transducer. Additional spin wave transducers shown are used for detecting the output signal and idler spin waves generated by the interaction between the input spin and the acoustic waves.

An interdigitated transducer excites the surface acoustic waves, the resulting strain from which modulates the magnetic anisotropy of the YIG film via magnetoelastic coupling and mediates the parametric interaction. ZnO serves as the piezoelectric material required for the transduction of electrical signals into acoustic waves. Devices with various angles for the spin wave transducers with respect to the acoustic wave are fabricated to investigate the angular dependence of the parametric interaction.

II. THEORY

Parametric pumping of spin waves by a traveling SAW is an example of nonlinear three-wave mixing in which the pump wave parametrically amplifies a signal wave and, in the process, produces a third idler wave. Conservation of energy and momentum requires the frequencies, ω, and wave vectors, $\boldsymbol{k}$, of the interacting waves to satisfy

$$\omega_p = \omega_s + \omega_i, \tag{1}$$

$$\boldsymbol{k}_p = \boldsymbol{k}_s + \boldsymbol{k}_i, \tag{2}$$

where the subscripts p, s, and i denote the pump, signal, and idler, respectively. Since the pump phonons carry momentum, the vector nature of (2) allows for the idler to propagate at an angle distinct from the signal wave.

In the degenerate case, the signal and idler frequencies are equal and exactly half of the pump frequency (i.e., $\omega_i = \omega_s = \omega_p/2$), satisfying (1). Assuming that the spin wave dispersion is isotropic in the film plane, the magnitudes of the signal and idler wave vectors will also be the same, i.e., $|\boldsymbol{k_s}| = |\boldsymbol{k_i}|$. Thus, to satisfy the vector sum in (2), the idler will travel away from the interaction region with angle

$$\theta_i = -\theta_s, \tag{3}$$

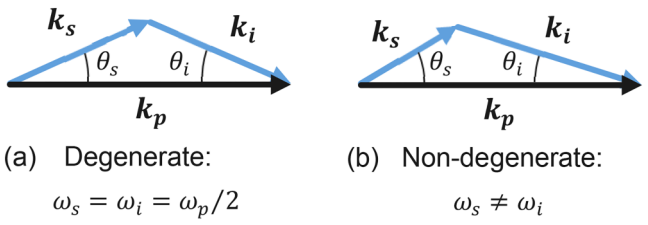

FIG. 2. Vector relation among signal, pump, and idler wavevectors for (a) degenerate and (b) non-degenerate cases.

where θ_i (θ_s) is the angle of incidence of the idler (signal) wave with respect to the pump [see Fig. 2(a)]. Accordingly, the degenerate case (2) can be re-stated as

$$|\boldsymbol{k_s}| = |\boldsymbol{k_i}| = |\boldsymbol{k_p}|/[2\cos(\theta_s)]. \tag{4}$$

We note that the assumption of isotropic spin wave dispersion is very nearly true for a ⟨111⟩ oriented YIG film under perpendicular bias, as is used in this work. The signal spin wave wavelengths, λ_s, required to match the condition of (4), are shown in Fig. 3(a) for varying angles of incidence and SAW wavelengths, λ_p. For increasing angles of incidence, shorter spin wave wavelengths are required for parametric interaction. This poses a challenge, in this work, of reliably patterning transducers for shorter wavelengths with the lithography capabilities available and limits the wavelengths and angles of incidence investigated experimentally.

Considering next, the non-degenerate case $\omega_s \neq \omega_i$ and $|\boldsymbol{k_s}| \neq |\boldsymbol{k_i}|$ as illustrated in Fig. 2(b). Consequently, shifting the

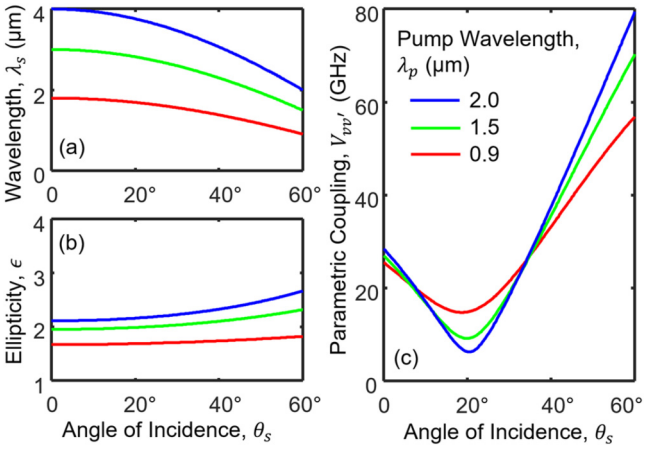

FIG. 3. The calculated (a) spin wave wavelength, λ_s, required to satisfy the wave vector condition of (4), (b) ellipticity, ϵ, of the signal spin wave, and (c) parametric coupling strength, $V_{vv'}$, between forward volume spin waves and SAWs as a function of the angle of incidence. The calculation for ellipticity and parametric coupling strength assumes a 1 μm thick ⟨111⟩ YIG film with M_s = 140 kA/m and anisotropy constants, K_1 = –610 J/m^3 and K_2 = –26 J/m^3.

signal or pump frequency will change not only the frequency but also the propagation direction of the idler.

The strength of the parametric coupling, $V_{vv'}$, depends on the angle of incidence of the signal spin waves on the SAWs. For forward volume spin waves, assuming uniform strain from the SAW through the thickness of the thin film, $V_{vv'}$, is given by[12,13]

$$V_{vv'} = i\gamma \frac{2B_1}{M_s} \frac{\tilde{u}_{xx}(\cos\theta_s + i\epsilon \sin\theta_s)^2 - i\tilde{u}_{zz}(1-\epsilon^2)\cos 2\theta_s}{2\epsilon}. \quad (5)$$

Here, $\tilde{u}_{xx}$ and $\tilde{u}_{zz}$ are, respectively, the amplitudes of the longitudinal and perpendicular strain components of the SAW; γ is the gyromagnetic ratio; B_1 and M_s are, respectively, the magnetoelastic coupling coefficient and saturation magnetization of the magnetic thin film; and ϵ is the ellipticity of spin precession (with $\epsilon = 1$ indicating circular precession). The ellipticity can be calculated[14] using $\epsilon = \omega_s/\gamma B_{\text{eff}}$ for an effective magnetic bias field B_{eff}, which includes the demagnetizing and anisotropy fields.

The right-hand term in the numerator of (5) gives the response to the strain component, $\tilde{u}_{zz}$, parallel to the equilibrium magnetization. As in parallel pumping with an RF field, this term is operative only if there is elliptical spin precession, resulting in a time-varying component of magnetization along the strain axis. The calculated ellipticity in 1 μm thick YIG for forward volume spin waves with wavelengths prescribed by (4) is plotted in Fig. 3(b) for several cases of SAW pump wavelength.

The left-hand term in the numerator is the response to the longitudinal strain component, $\tilde{u}_{xx}$, perpendicular to the magnetization. The action of $\tilde{u}_{xx}$ is different from a perpendicular RF field because the induced time-varying anisotropy has an *axis* rather than a *direction*. As a result, magnetization precession is forced *twice* in an acoustic cycle, and the parametric pumping of even circularly precessing moments becomes possible.

These two pumping terms in (5) can either reinforce or counteract each other depending on the angle of incidence as well as the magnitude and relative phase between the strain components of the acoustic wave. On the surface of ⟨111⟩ cut YIG, for example, the longitudinal and perpendicular strain components of an SAW are related by[15] $\frac{\tilde{u}_{zz}}{\tilde{u}_{xx}} = -0.42$, yielding the angular variation of the parametric coupling strength, $V_{vv'}$, as plotted in Fig. 3(c). In this case, the pumping effects of $\tilde{u}_{xx}$ and $\tilde{u}_{zz}$ strain components counteract each other around 20° leading to a minimum in coupling. At angles of incidence above 40°, the two terms reinforce each other, and the parametric coupling strength significantly exceeds that of the collinear ($\theta_s = 0°$) arrangement. Thus, in a YIG film with the given properties, large angles of incidence are desirable for pumping forward volume spin waves with SAWs.

III. MICROMAGNETIC SIMULATION

Micromagnetic simulations of the interaction are performed at 0 K in MuMax3[16] software. The SAW is simulated as a spatially and temporally varying strain of 4 GHz frequency (0.9 μm wavelength). The relative amplitudes and phase of the longitudinal (ϵ_{xx} and ϵ_{zz}) and shear (ϵ_{xz}, ϵ_{yz} and ϵ_{xy}) strain components used are for SAWs traveling in ⟨111⟩ cut YIG,[15]

$$\begin{aligned}
\epsilon_{xx} &= A\sin(\omega_p t - k_p x),\\
\epsilon_{zz} &= 0.420A\sin(\omega_p t - k_p x + \pi),\\
\epsilon_{xz} &= 0.002A\sin\left(\omega_p t - k_p x + \frac{\pi}{2}\right),\\
\epsilon_{xy} &= 0.071A\sin\left(\omega_p t - k_p x + \frac{\pi}{2}\right),\\
\epsilon_{yz} &= 0.012A\sin\left(\omega_p t - k_p x + \frac{\pi}{2}\right),
\end{aligned} \quad (6)$$

where A is the strain amplitude of the SAW.

The properties assumed for the YIG film are saturation magnetization, $M_s = 140$ kA/m; damping constant[17] 10^{-4}; magnetoelastic coupling coefficients[18] $B_1 = 0.35$ MJ/m^3 and $B_2 = 0.7$ MJ/m^3; exchange stiffness 2 pJ/m; and first and second order anisotropy constants[14] −610 and −26 J/m^3, respectively, in a ⟨111⟩ crystal orientation. The spin wave is excited at 2 GHz (i.e., at exactly half pump frequency). An out-of-plane bias field between 199 and 203 mT is imposed to obtain the requisite spin wave wavelength at different angles of incidence per (4).

The simulation results are presented in Fig. 4. The steady state spin waves, after 1 μs of simulation time, are shown as a color scale corresponding to the x-component of magnetization. In the collinear case, Fig. 4(c), amplification of the spin wave can clearly be seen in comparison to the un-pumped spin wave decay in Fig. 4(b). For each angle of incidence simulated, an idler spin wave appears at the expected symmetrical angle [Figs. 4(d)–4(h)]. Consistent with the theoretical results discussed in Sec. II, the idler is weak for the 20° angle of incidence and gets progressively stronger at higher angles.

Plotted in Figs. 5(a) and 5(b), respectively, are the signal and idler gain as a function of SAW strain amplitude. The signal (idler) gain is defined as the ratio of the amplitude of the signal (idler) spin wave measured at the signal (idler) output to a fixed amplitude at the input. The amplitudes are calculated by determining the magnetization within a 0.01 GHz bandwidth around 2 GHz and averaging over a line at the corresponding output locations, as marked in Fig. 4(a). The lines are the same length as the input transducers. As seen from Fig. 5(a), at low SAW (pump) amplitudes, the signal gain is less than 1 due to spin wave decay. The attenuation is overcome by parametric pumping at higher SAW amplitudes (except for the 20° angle of incidence), with the increase in signal gain occurring at lower SAW amplitudes for higher angles of incidence as expected from theory. The observation of an idler in the 20° case [Fig. 5(b)] indicates that parametric pumping takes place, but the coupling strength is insufficient to overcome the decay.

A measure of the coupling strength may be obtained by considering the SAW amplitude at which a signal gain of unity is achieved. This threshold SAW amplitude, u_{th}, should be inversely proportional to the coupling strength via

$$u_{th} = \Gamma/|V_{vv'}(\theta_s)|, \quad (7)$$

where $\Gamma = \alpha\omega_s$ is the spin wave damping rate at frequency ω_s in a material with damping parameter α. The coupling strength thus

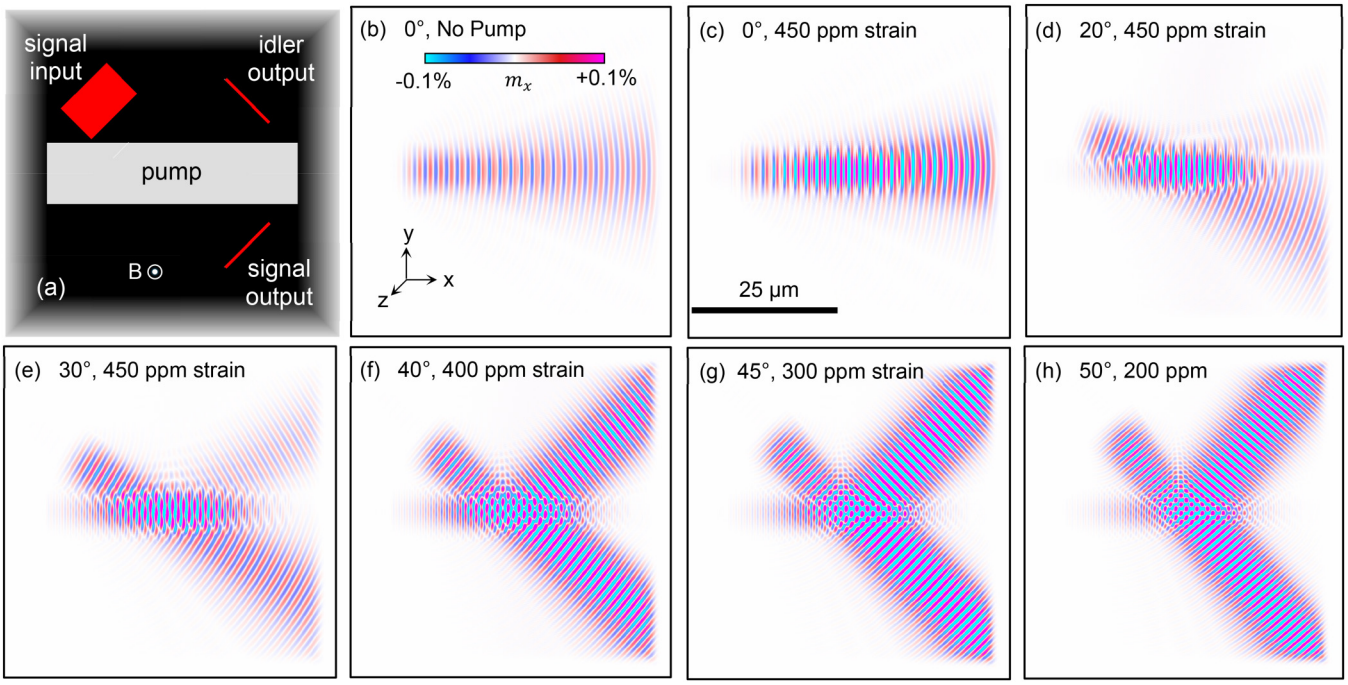

FIG. 4. (a) Illustration of setup for micromagnetic simulations shown, as an example, for 45° angle of incidence. The interaction is simulated for a 50 × 50 × 1 μm^3 YIG film using a mesh of 2048 cells × 2048 cells. The black region represents the simulation area with the shaded border representing increasingly higher damping at the edges to eliminate spin wave reflection. A spin wave of 10 μm beam width is generated at the location marked as the "signal input." The amplitudes for the signal and idler spin waves are measured at the "signal output" and the "idler output," respectively. The SAW pump is mimicked by imposing a temporally and spatially varying strain wave of 10 μm beam width, traveling from left to right in the region marked "pump." (b) Simulation of the spin wave without an SAW pump. The color bar indicates the x-component of magnetization (normalized to M_s). (c)–(h) Simulations at varying angles of incidence and SAW strain amplitude, A, as indicated. The SAW strain amplitude must be reduced for the higher incidence angles to avoid secondary nonlinear effects from the larger parametric coupling strength at these angles. All simulations shown are for the degenerate case, with the acoustic pump and spin wave frequencies fixed at 4 and 2 GHz, respectively.

determined is plotted in Fig. 5(c) for varying angles of incidence and qualitatively agrees with the behavior predicted by theory [solid trace in Fig. 5(c)]. (For angles near 20°, $V_{vv'}$ cannot be determined as the signal gain does not reach unity.) It should be noted that unlike the simulations, the theoretical model assumes infinite plane waves.

IV. EXPERIMENTS

The devices consist of acoustic- and spin-wave transducers fabricated atop a 425 nm thick ZnO film sputtered on YIG/GGG substrates (Innovent e.V., Germany). The YIG film is 1 μm thick, grown by liquid phase epitaxy on 500 μm thick ⟨111⟩ cut GGG.[17] The thickness of the ZnO film is a trade-off between obtaining good crystalline structure for piezoelectric properties and minimizing the separation between the transducers and the YIG film so that both spin waves and strain are present through the depth of the YIG film for the desired magneto-acoustic interaction.

The transducers are patterned in 160 nm thick Al layers evaporated on the ZnO with a 5 nm Ti adhesion layer. A top view of a device with a collinear arrangement of the acoustic- and spin wave transducers is shown in Fig. 6(a). Devices with spin wave transducers at 0°, 30°, and 45° to the acoustic transducers were fabricated. The acoustic transducers are designed as uniform IDTs with 50 finger pairs of 70 μm length and a finger-to-finger spacing of 0.75 μm to generate acoustic waves of 1.5 μm wavelength. Assuming an SAW velocity of ∼3000 m/s in the ZnO/YIG films, the center frequency of the IDTs is expected to be ∼2000 MHz. The spin wave transducers are meandering coplanar ground-signal-ground waveguides with six meanders, each of 33.75 μm length. The wavelength of the spin waves excited (or detected) equals twice the conductor-to-conductor spacing, which varies with the angle of the spin wave transducer such that the design satisfies $\lambda_s = 2\lambda_p \cos(\theta_s)$ per (4). Figures 6(b) and 6(c) show examples of scanning electron microscope images of the acoustic- and spin wave transducers.

The setup for investigating the parametric pumping of spin waves with the fabricated devices is illustrated in Fig. 7. A magnetic bias field is applied perpendicular to the YIG film to support spin waves in the forward volume mode. The IDT is driven at a fixed frequency f_p = 2048.2 MHz. The signal spin wave frequency, f_s, is varied around 1024.1 MHz (i.e., around $f_p/2$). The bias field strength is

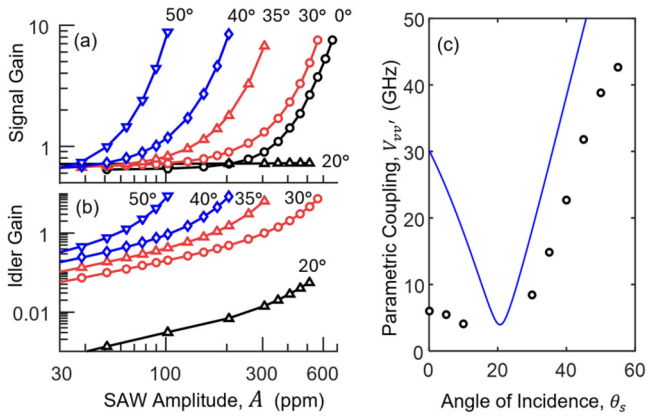

FIG. 5. (a) Signal and (b) idler gain as a function of SAW pump amplitude for various angles of incidence between the SAW and the signal spin wave. (Reproduced with permission from C. Rivard, A. Jander, and P. Dhagat, IEEE Magn. Lett. **15**, 5500205 (2024). Copyright 2024, IEEE.) (c) Parametric coupling strength obtained from simulations (open circles) and the analytical expression in Eq. (5) (solid trace). Simulation results shown are for a 200 × 200 × 1 μm^3 YIG film discretized into 8192 cells × 8192 cells. (i.e., 4× larger area than used for Fig. 4 but with identical mesh density). The SAW and spin wave beam widths are 40 μm.

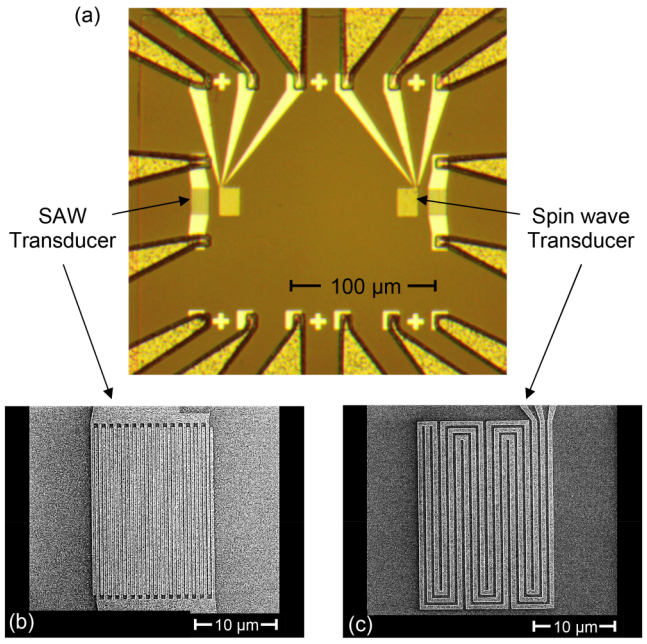

FIG. 6. (a) Optical microscope image of a device with the acoustic and spin wave transducers in a collinear arrangement. The contacts in the periphery lead to ground-signal-ground probe pads not seen in the image. Electron microscope images of (b) the acoustic transducer designed as a uniform IDT and (c) the spin wave transducer designed as a meandering coplanar ground-signal-ground waveguide.

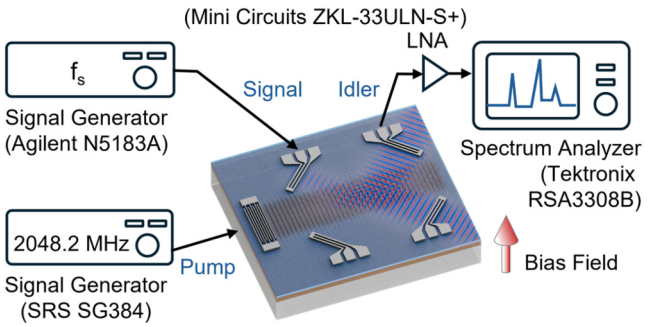

FIG. 7. Experimental setup for measuring the parametric pumping of forward volume spin waves by surface acoustic waves. The "pump" and "signal" transducers are driven by separate microwave signal generators. The signal detected at the "idler" output transducer is amplified using a low-noise amplifier (LNA) and observed on a spectrum analyzer.

adjusted to tune the spin wave dispersion such that the spin wave wavelength at $f_p/2$ matches twice the conductor-to-conductor spacing on the transducer. The spectrum of the idler wave resulting from the interaction between the acoustic wave and the signal spin wave is measured at the idler output transducer for each f_s using a spectrum analyzer. A low-noise amplifier is used to reduce the input noise level to below −160 dBm.

Shown in Fig. 8(a) are the idler wave spectra obtained for $f_s = 1024.1$ MHz (degenerate), 1010.1 MHz, and 1030.1 MHz (non-degenerate) on a device with the spin wave transducer at 30°. The stronger peak in each of the three traces corresponds to the signal spin wave frequency, which feeds through due to the electromagnetic coupling between the spin wave transducers. The smaller peaks are the idler (ignoring the spurious peak at 1025 MHz from interference in the laboratory). For the degenerate case, the idler is present at the same frequency, $f_p/2$, as the feedthrough, and hence, not discernible. In the non-degenerate case, the idler is seen at a different frequency from the signal spin wave or feedthrough frequency, showing the spectral separation of the spin waves possible via parametric interaction with the surface acoustic waves. We note that the idler is observed only when the bias field is set precisely for the propagation of spin waves with the wave vectors determined by (4). If the field is de-tuned, the idler disappears, confirming that the detected electrical signal originates from a spin wave rather than spurious intermodulation in the electronics. The parametrically amplified signal spin wave, which travels to the opposing output transducer, could not be distinguished from the feedthrough at the same frequency in the current experimental setup. The amplification of the signal spin wave is, therefore, not investigated.

Figure 8(b) shows the idler power and frequency obtained from the spectra as a function of the signal spin wave frequency. At each signal frequency, the sum of the idler and the signal spin wave frequencies equals the acoustic pump frequency in agreement with (1). Note that the spectra in Fig. 8(a) are line cuts of this plot at $f_s = 1010.1$, 1024.1, and 1030.1 MHz. The range of detectable idler frequencies is limited by the bandwidth of the spin wave transducer. Accordingly, the idler power is seen to decrease further

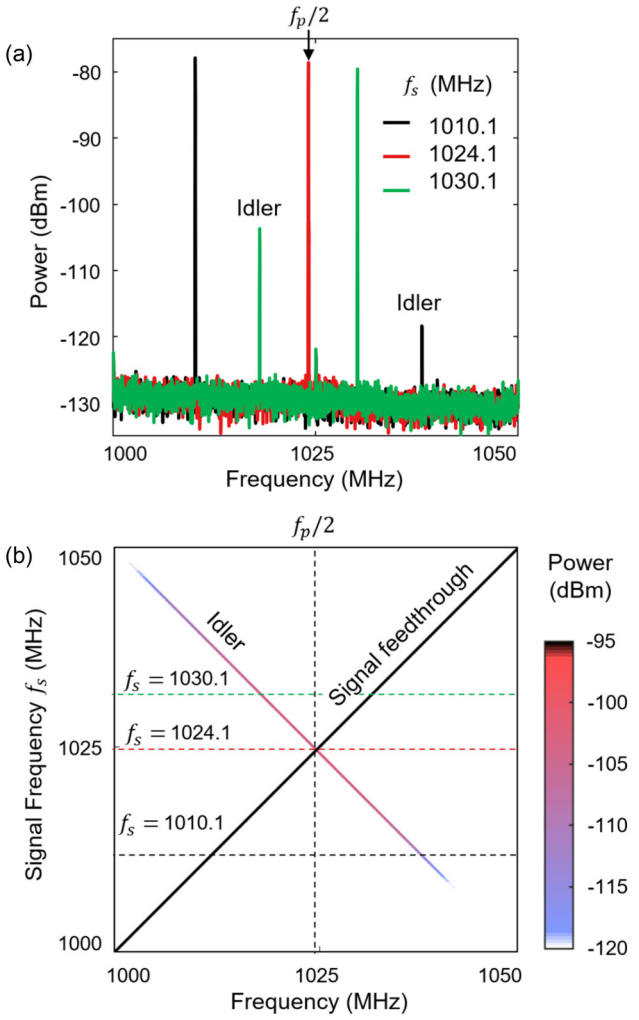

FIG. 8. (a) Idler spectra corresponding to the signal spin wave frequencies of 1010.1, 1024.1, and 1030.1 MHz. For the degenerate case (i.e., for 1024.1 MHz), the idler and signal feedthrough are superposed and, hence, indistinguishable. (b) Idler power (color bar) and frequency (x axis) as the signal spin wave frequency is varied from 1000 to 1050 MHz. The data shown are for a device with $\theta_s = 30°$; $\lambda_p = 1.5\,\mu$m; $f_p = 2048.2$ MHz; SAW power = 16 dBm; bias field = 179.5 mT; and spin wave power = −15 dBm.

away from degeneracy. These data are representative of observations on other devices with different angles of spin wave incidence.

In the left-hand plots in Figs. 9–11, idler power is shown as a function of SAW and signal spin wave power for different devices. Details of the devices and experimental settings are noted in the figure captions. (SAW power refers to the electrical power applied to the IDT, not the power in the acoustic wave.) The signal spin wave frequency is set at 1024.099 MHz, very close to the degenerate condition, but offset by 1 kHz to allow for discrimination of the idler from the feedthrough. The idler power is seen to rise above the −160 dBm input noise level at the spectrum analyzer and then,

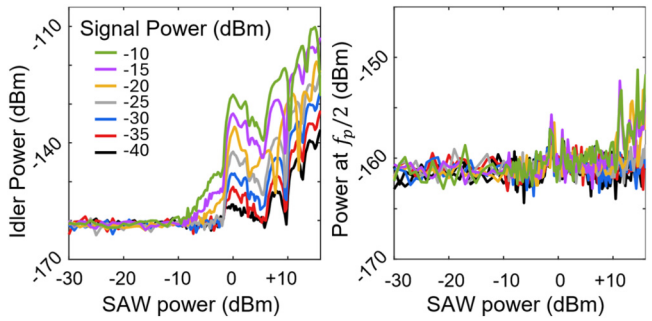

FIG. 9. (Left) Detected idler power vs SAW power for different power levels of a signal spin wave at 0° angle of incidence, with $\lambda_p = 1.5\,\mu$m, $\lambda_s = 3.0\,\mu$m, $f_p = 2048.2$ MHz, $f_s = 1024.099$ MHz, and bias field = 180.3 mT. (Right) Power detected at exactly half of the pump frequency for the same conditions.

as expected from the bilinearity of the parametric interaction, increases with the SAW as well as the signal power. A quantitative comparison of the interaction strength for the different angles of incidence investigated is not possible due to the differences in transducer efficiency resulting from their design (conductor widths and spacing).

In all devices, the bilinear response to the signal and SAW power is seen up to an SAW power of about −2 dBm, beyond which the response becomes chaotic, presumably due to the appearance of a parametric instability, i.e., the amplification of spin waves from the thermal background. Since the spin waves generated from the thermal background do not necessarily match the wave vector selectivity of the spin wave transducers, they are difficult to observe directly. Evidence of the parametric instability can, however, be inferred by the presence of a signal at the idler output at exactly half of the pump frequency (i.e., degenerate condition). For example, in a device with a 30° angle of incidence, a signal, independent of the input spin wave power, is seen to emerge at around −2 dBm SAW power [Fig. 10 (right)]. The excitation of

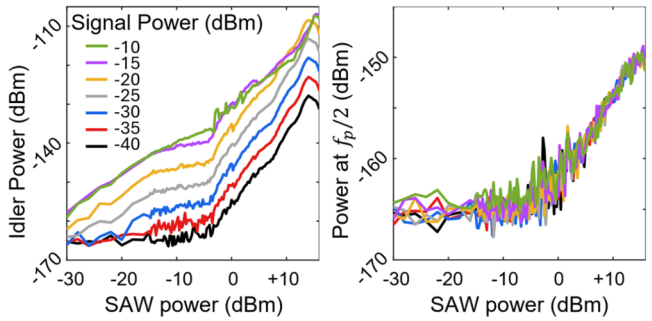

FIG. 10. (Left) Detected idler power vs SAW power for varying power levels of a signal spin wave at 30° angle of incidence, with $\lambda_p = 1.5\,\mu$m, $\lambda_s = 2.6\,\mu$m, $f_p = 2048.2$ MHz, $f_s = 1024.099$ MHz, and bias field = 179.5 mT. (Right) Power detected at exactly half of the pump frequency for the same conditions.

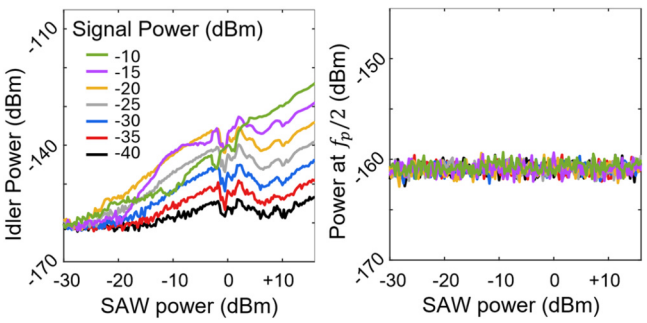

FIG. 11. (Left) Detected idler power vs SAW power for varying power levels of a signal spin wave at 45° angle of incidence, with $\lambda_p = 2.0\,\mu$m, $\lambda_s = 2.83\,\mu$m, $f_p = 1601$ MHz, $f_s = 800.499$ MHz, and bias field = 175.0 mT. (Right) Power detected at exactly half of the pump frequency for the same conditions.

spin waves unrelated to the signal spin wave can also be seen in the collinear device [Fig. 9 (right)]. In a device with a 45° angle of incidence, however, a signal at $f_p/2$ is not observed despite a disturbance seen in the idler at around −2 dBm pump power (Fig. 11).

A direct measure of the SAW strain amplitude, A, was not available to facilitate the comparison of experimental data with the theory and micromagnetic simulations. However, based on electrical reflection (S_{11}) measurements of the IDTs, an estimated 6% of the applied electrical power is converted into acoustic waves traveling to the right from the transducer. Thus, at −2 dBm applied power, the SAW strain amplitude is estimated to be ∼120 ppm[19]—comparable to the threshold strain amplitude seen in micromagnetic simulations for overcoming spin wave decay at higher angles of incidence [$\geq 40°$ in Fig. 5(a)]. Together, the theory, modeling, and experimental results suggest that true, continuous amplification of forward volume spin waves can be achieved with SAW pumping.

V. CONCLUSION

In this work, we have demonstrated the parametric pumping of coherent forward volume spin waves by traveling surface acoustic waves in a thin-film yttrium iron garnet device. In theory, micromagnetic modeling and experimental results that deepen understanding of the nonlinear three-wave mixing interaction are presented. The experimental data exhibit qualitative agreement with theoretical predictions and micromagnetic simulations. The energy and momentum imparted to the spin wave by the SAW can result in frequency translation and angular deflection of the idler spin wave. For the conditions investigated, high angles of incidence between the spin wave and the SAW pump are desirable to achieve strong parametric coupling between the forward volume spin waves and SAWs. The experimental data provide evidence that parametric *amplification* of the spin waves should be possible at an SAW pump amplitude below the threshold of instability for the pumping of thermal spin waves. These results establish a practical vision for utilizing magneto-acoustic interactions for device applications in wave-based signal processing and computation.

AUTHOR DECLARATIONS

Conflict of Interest

The authors have no conflicts to disclose.

Author Contributions

Albrecht Jander: Conceptualization (lead); Supervision (equal); Writing – original draft (lead); Writing – review & editing (equal). **Pallavi Dhagat:** Conceptualization (supporting); Project administration (equal); Resources (equal); Supervision (equal); Writing – review & editing (equal). **Carson Rivard:** Formal analysis (equal); Investigation (lead); Methodology (lead); Writing – original draft (supporting).

DATA AVAILABILITY

The data that support the findings of this study are available from the corresponding author upon reasonable request.

REFERENCES

[1]B. A. Kalinikos and M. P. Kostylev, "Parametric amplification of spin wave envelope solitons in ferromagnetic films by parallel pumping," IEEE Trans. Magn. **33**(5), 3445–3447 (1997).
[2]P. A. Kolodin, P. Kabos, C. E. Patton, B. A. Kalinikos, N. G. Kovshikov, and M. P. Kostylev, "Amplification of microwave magnetic envelope solitons in thin yttrium iron garnet films by parallel pumping," Phys. Rev. Lett. **80**(9), 1976–1979 (1998).
[3]T. Brächer, P. Pirro, and B. Hillebrands, "Parallel pumping for magnon spintronics: Amplification and manipulation of magnon spin currents on the micron-scale," Phys. Rep. **699**, 1–34 (2017).
[4]R. Verba, V. Tiberkevich, I. Krivorotov, and A. Slavin, "Parametric excitation of spin waves by voltage-controlled magnetic anisotropy," Phys. Rev. Appl. **1**(4), 044006 (2014).
[5]P. Chowdhury, P. Dhagat, and A. Jander, "Parametric amplification of spin waves using acoustic waves," IEEE Trans. Magn. **51**(11), 1300904 (2015).
[6]P. Chowdhury, A. Jander, and P. Dhagat, "Nondegenerate parametric pumping of spin waves by acoustic waves," IEEE Magn. Lett. **8**, 3108204 (2017).
[7]S. G. Alekseev, S. E. Dizhur, N. I. Polzikova, V. A. Luzanov, A. O. Raevskiy, A. P. Orlov, V. A. Kotov, and S. A. Nikitov, "Magnons parametric pumping in bulk acoustic waves resonator," Appl. Phys. Lett. **117**(7), 072408 (2020).
[8]H. Matthews and F. R. Morgenthaler, "Phonon-pumped spin-wave instabilities," Phys. Rev. Lett. **13**(21), 614–616 (1964).
[9]D. H. Lyons, H. Matthews, and F. R. Morgenthaler, "Parametric excitation of spin waves by phonon pumping," J. Appl. Phys. **44**(3), 1348–1355 (1973).
[10]M. Geilen, R. Verba, A. Hamadeh, A. Nicoloiu, D. Narducci, A. Dinescu, M. Ender, M. Mohseni, F. Ciubotaru, M. Weiler, A. Müller, B. Hillebrands, C. Adelmann, and P. Pirro, "Parametric excitation and instabilities of spin waves driven by surface acoustic waves," Adv. Phys. Res. **4**(1), 2400086 (2025).
[11]M. Mohseni, A. A. Hamadeh, M. Geilen, and P. Pirro, "Amplification and frequency conversion of spin waves using acoustic waves," IEEE Trans. Nanotechnol. **22**, 806–810 (2023).
[12]C. Rivard, A. Jander, and P. Dhagat, "Micromagnetic modeling of parametric amplification of forward volume spin waves by noncollinear surface acoustic waves," IEEE Magn. Lett. **15**, 5500205 (2024).
[13]I. Lisenkov, A. Jander, and P. Dhagat, "Magnetoelastic parametric instabilities of localized spin waves induced by traveling elastic waves," Phys. Rev. B **99**(18), 184433 (2019).

[14]D. D. Stancil and A. Prabhakar, *Spin Waves: Theory and Applications* (Springer, 2009).
[15]A. J. Slobodnik, R. T. Delmonico, and E. D. Conway, *Microwave Acoustics Handbook* (Air Force Cambridge Research Laboratories, 1974), Vol. 2.
[16]A. Vansteenkiste, J. Leliaert, M. Dvornik, M. Helsen, F. Garcia-Sanchez, and B. Van Waeyenberge, "The design and verification of MuMax3," AIP Adv. **4**(10), 107133 (2014).
[17]C. Dubs, O. Surzhenko, R. Linke, A. Danilewsky, U. Brückner, and J. Dellith, "Sub-micrometer yttrium iron garnet LPE films with low ferromagnetic resonance losses," J. Phys. D: Appl. Phys. **50**(20), 204005 (2017).
[18]A. B. Smith and R. V. Jones, "Magnetostriction constants from ferromagnetic resonance," J. Appl. Phys. **34**(4), 1283–1284 (1963).
[19]W. P. Robbins, "A simple method for approximating surface acoustic wave power densities," IEEE Trans. Sonics Ultrason. **24**(5), 339 (1977).